6.3   **Sensitivity of orographic precipitation to changing ambient conditions:**

An idealized modeling perspective

Brian A. Colle[*]

Institute for Terrestrial and Planetary Atmospheres, Stony Brook University/SUNY

1. INTRODUCTION

Cool season precipitation forecasting in mountainous terrain is challenging since the distribution and amount of precipitation is controlled by a number of dynamical and microphysical processes. It is commonly known that moist flow ascending a mountain barrier (i.e., upslope flow) will typically enhance the precipitation along the windward slope. Both modeling (Sinclair 1994, among others) and observational (Pandey et al. 1999, among others) studies have shown that the magnitude of the upslope flow typically determines how much precipitation will fall. However, there are other factors that may determine the amount and distribution of orographic precipitation, such as the thermodynamic stratification, moisture availability, wind profile above the barrier, as well as hydrometeor advection and generation rates. For example, recent studies have investigated the role of flow blocking in enhancing the upstream orographic precipitation distribution as determined by the Froude number, $U/(h_m N)$ (Sinclair 1994; Neiman et al. 2002), the importance of gravity waves in hydrometeor production above narrow ridges (Bruintjes et al. 1994), and the importance of microphysical timescales (Jiang and Smith 2002).

There have been many idealized studies investigating the interaction of dry dynamics with topography at all scales, but much less attention has been given to moist flow dynamics and its influence on orographic precipitation. In order to better understand the factors that effect orographic precipitation, both 2-D and 3-D an idealized modeling approaches are necessary. For many elongated barriers, such as the California Sierras, Colorado Front Range, and the France Pyrenees, 2-D numerical modeling has been shown to be an effective tool to understand the terrain flow interaction; therefore, this approach was utilized in many of our experiments. Some 3-D simulations have also been completed for more complex terrain such as the Wasatch Mountains of Utah and the California coastal range.

2. MODEL SETUP

The Penn State/NCAR mesoscale model (MM5v3) was run in a 2-D idealized configuration using a 500 grid point long domain with 4-km horizontal grid spacing, 39 sigma levels, and constant lateral boundary conditions. The parameters defined during model initialization include the barrier height (h_m), mountain half width (L) for a bell-shaped barrier, upstream flow velocity (U), moist static stability (N_m), and freezing level (FL). The moisture initialization was specified to be nearly saturated (99% relative humidity) throughout the domain, therefore the initial static stability (N_m) in this study is defined relative to moist processes (Durran and Klemp 1982). The MM5 was integrated using the Reisner2

[*]Corresponding author address: Dr. Brian A. Colle, Marine Sciences Research Center, Stony Brook University, Stony Brook, NY 11794-5000. email: bcolle@notes.cc.sunysb.edu.

(includes mixed phase and graupel) explicit scheme and MRF PBL (with no heat/moisture surface fluxes). Klemp and Durran's (1983) upper-radiative boundary condition and a sponge layer were applied in order to prevent gravity waves from being reflected off the model top. The 2-D runs included rotational effects ($f \sim 10^{-4}$ s^{-1}), therefore terrain-normal flow can develop when a pressure gradient exists in the x-direction. Below are how the parameters were varied:

U = 5, 10, 15, 20, 25, and 30 m s^{-1}.
h_m = 500, 1000, 1500, 2000, and 2500 m.
N_m = 0.005 and 0.01 s^{-1}.
L = 50 and 25 km.
FL = slightly below surface (sea-level temperature = 270 $^\circ$K, FLSFC), at 750 mb (FL750), and at 500 mb (FL500).

3. ROLE OF THE MOUNTAIN CIRCULATION

For the first set of experiments both L and FL were fixed at 50 km and 750 mb, respectively. Figure 1 shows the accumulated 6-12 h precipitation across the barrier for a fixed ambient wind speed but slowly increasing mountain height. As a result, the variations in Froude number are determined by changes in barrier height. For the simulations using U =10 m s^{-1} and N_m,=0.01 s^{-1} (Fig. 1a), the precipitation distribution is broad and decreases
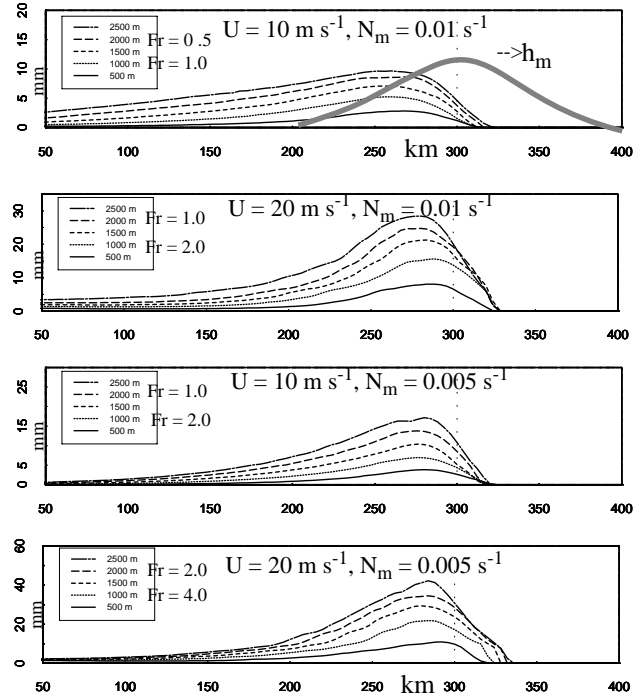
Figure 1. Accumulated precipitation (6-12 h) as a function of terrain height (see inset box) for (a) 10 m s^{-1}, N_m = 0.01 s^{-1} and (b) 20 m s^{-1}, N_m = 0.01 s^{-1}. (c) and (d) Same as (a) and (b) except for N_m = 0.005 s^{-1}. The thick gray line is the mountain location.

gradually upstream of the barrier. As the barrier height is increased from 500 to 1500 m the precipitation maximum shifts slightly upstream, while the maximum precipitation increase from h_m = 2000 to 2500 m occurs ~150 km upstream of the crest because of flow blocking (Fr < .5). When the flow is increased to 20 m s^{-1} (Fig. 1b), more precipitation occurs over the upper windward slope even for fairly low Froude numbers (Fr ≤ 1). Similarly, for N=0.005 s^{-1} and 10 m s^{-1} (Fig. 1c,d), the precipitation profiles for Fr ≤ 1 are peaked more over the upper windward slope than the Fr ≤ 1 runs for N_m =0.01 s^{-1}. Overall, the shape of the cross barrier precipitation distribution is more similar between runs of similar U or N_m than Fr.

Figure 2a shows how the 6-12 h cross mountain precipitation profile for h_m = 1500 m, N = 0.01 s^{-1}, and L = 50 km varies as a function of ambient wind speed. The thick arrow indicates where along the x-axis the precipitation increases most rapidly for each 5 m s^{-1} increase. As the flow increases from 5 to 20 m s^{-1}, there is downstream shift in precipitation towards the crest, with little increase in precipitation more than 50 km upwind of the crest. In contrast, for strong wind speeds (> 25 m s^{-1}), the precipitation enhancement shifts more *upwind* of the barrier. Figure 3 presents the mountain circulation and precipitation species (rain, snow and graupel) for these series of wind speed experiments in Fig. 2a. For

relatively weak flow (10 m s^{-1}), the calculated and simulated vertical wavelengths of the terrain-induced gravity wave ($\lambda_z = 2\pi U/N_m$) are 6.3 and 7.5 km, respectively. This wave results weak downward motion over the windward slope above 4 km and over the crest, which results in a shallow orographic cloud over the windward side of the barrier. When the wind speed is doubled (20 m s^{-1}), λ_z doubles and the region of mountain-wave subsidence over the crest rises to above 4 km, which allows for more upward motion and precipitation above the upper windward slope and crest. For U = 30 m s^{-1} (Fig. 3c), the large vertical wavelength (~25 km) results in a deep area of significant rising motion over the windward slope, thus the precipitation area builds back *upstream* of the barrier again. These systematic changes in mountain circulation and cross mountain precipitation (Fig. 1) are similar for other terrain heights since λ_z is independent of h_m. Overall, these results suggest the horizontal precipitation distribution for L=50 km is strongly effected by the vertical structure of the mountain wave circulation.

Figure 2. Accumulated precipitation (6-12 h) versus wind speed (m s^{-1}) for h_m =1500 m for experiments of varying mountain width (L), stability (N_m), and freezing level (FL). The text on panels a-e list the parameters used in each series of experiments. The dashed line shows the mountain crest.
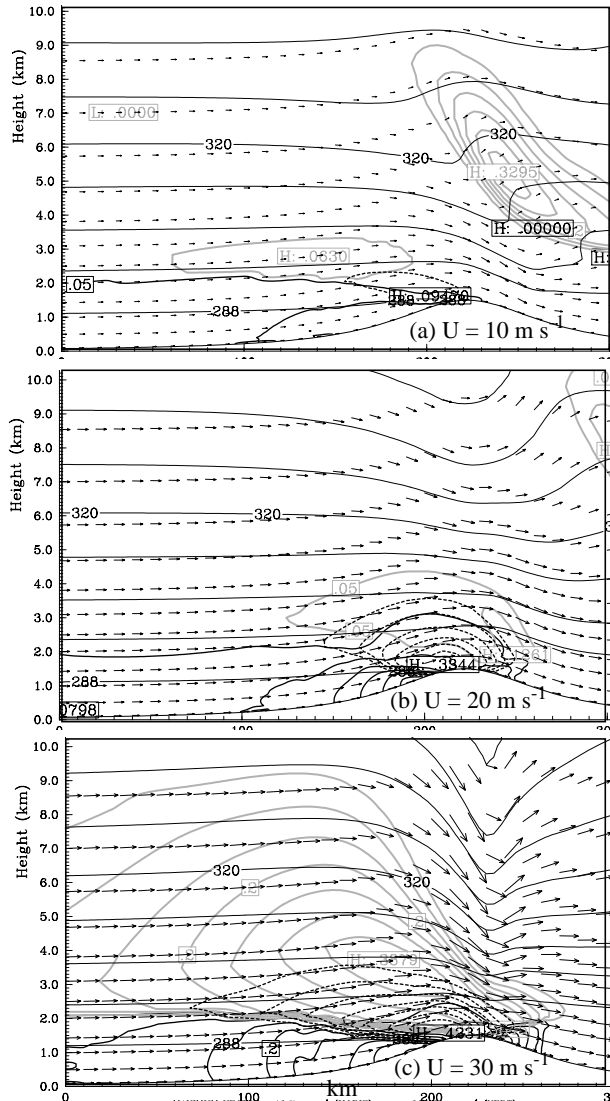
Figure 3. Cross mountain profile (h_m=1500 m; L = 50 km) of potential temperature (thin solid), wind vectors, snow (gray), graupel (dashed), and rain (solid) for U = (a) 10 m s^{-1}, (b) 20 m s^{-1}, and (c) 30 m s^{-1}.
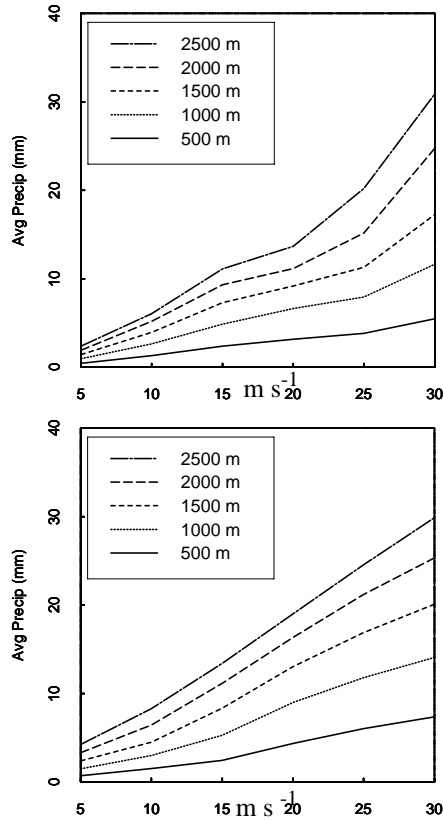
Figure 4. Average precipitation 100 km upstream of the crest to 50 km in the lee for h_m = 500 to 2500 m versus wind speed for (a) N_m=.01 s^{-1}, L= 50 km and (b) N_m=.005 s^{-1}, L= 50 km.

Figure 4a presents the average precipitation for the region 100 km upstream of the crest to 50 km in the lee as a function of ambient wind speed for the L=50 km and $N_m = 0.01$ s^{-1}. The precipitation amounts increase rapidly as U increases to 15 m s^{-1} for many barrier heights, but between 15-20 m s^{-1} the increase slows as the mountain wave begins building upstream. As the upward motion with the vertical-propagating gravity wave deepens over the windward slope for U> 20 m s^{-1} (Fig. 3c), the precipitation increases more rapidly again.

When N_m is reduced to 0.005 s^{-1} (Fig. 2b), the upwind shift of precipitation increase occurs between 10 and 15 m s^{-1} rather the 25 to 30 m s^{-1} for N_m=0.01 s^{-1}. This is consistent with λ_z increasing more rapidly with increasing wind speed for N_m=0.005 s^{-1}, resulting in a more rapid buildup of precipitation upstream of the crest compared to $N_m = 0.01$ s^{-1}. However, since the flow is less stable for $N_m = 0.005$ s^{-1}, vertically propagating gravity waves have less upstream tilt (ϕ) above the crest for high wind speeds compared to $N_m = 0.01$ s^{-1} ($N_m \cos\phi = Uk_m$, where k_m is the mountain wave number). Thus, for less stable flow there is more upward motion and precipitation over the crest at high windspeeds and a downstream shift in precipitation towards the lee. For $N_m = 0.005$ s^{-1} the average precipitation over the barrier increases nearly linearly with increasing wind speed for moderate to high barriers (Fig. 4b). This is consistent with recent observational studies under near moist neutral conditions (Neiman et al. 2002).

4. ROLE OF MOUNTAIN WIDTH AND FREEZING LEVEL

The mountain half-width (L) was decreased from 50 to 25 km to address the effects of mountain steepness for $N_m = 0.01$ s^{-1} and FL = 750 mb. A steeper barrier favors a more narrow precipitation distribution (Fig. 2c), with the maximum at the crest for U > 15 m s^{-1}. For increasing moderate windspeeds (15 to 30 m s^{-1}) the windward precipitation amounts do not change significantly (Fig. 2c), which suggests a balance between additional windward condensate generated upwind of the crest and the advection precipitation into the lee by the stronger winds.

A series of simulations were completed using $N_m = 0.01$ s^{-1} and L = 50 km, but the freezing level (FL) was increased to 500 mb (Fig. 2c). For these higher freezing level experiments the orographic cloud is dominated by warm rain processes. A higher freezing level results in a more narrow peak of precipitation over the steep windward slope compared to the lower freezing level runs (Figs. 2a). The higher freezing level also results in a more rapid increase in precipitation rate with increasing wind speed between 15-25 m s^{-1}, less rapid increase between 25-30 m s^{-1}, and there is less precipitation spillover into the lee.

When the freezing level is lowered to just below sea level for N_m=0.01 s^{-1} and L=50 km (FLSFC, Fig. 2c), the the precipitation distribution is more similar to FL750 than FL500, but for high wind speeds the FLSFC precipitation is less broad than FL750 since most of the snow growth occurs at low-levels immediately over the windward slope given the very cold temperatures aloft. This results in more snow falling out closer to the crest than FL750.

5. ROLE OF VERTICAL WIND SHEAR ABOVE BARRIER

Changes in the ambient winds above crest level may also effect the precipitation distribution. Therefore, two sensitivity runs were completed in which the winds at or below crest level (1500 m) were initialized at 15 m s^{-1}, but either reverse or forward shear was specified above the barrier. For the reverse shear initialization the ambient flow decreased linearly above the crest to zero at 550 mb, while for forward shear the winds increased to 30 m s^{-1} at 550 mb. These sensitivity runs were initialized with $N_m = 0.01$ s^{-1} and L = 25 km.

Figure 5 shows the 6-12 h precipitation across a 1500 m barrier for the control (no shear), reverse, and forward shear simulations. Reverse shear above the barrier favors low-level mountain wave amplification and therefore more subsidence over the crest and lee (not shown), which in turn reduces the precipitation in this region relative to no shear and forward shear cases. Decreasing winds above the crest also increases precipitation 50-100 km upstream of the crest through perhaps longer time scales for ice growth aloft. In contrast, forward shear favors a weaker vertically propagating gravity wave (not shown), therefore reducing the upward motion and precipitation production aloft over the windward slope. Furthermore, the stronger flow aloft with forward shear also results in slightly more precipitation advecting 10-20 km downwind of the crest.
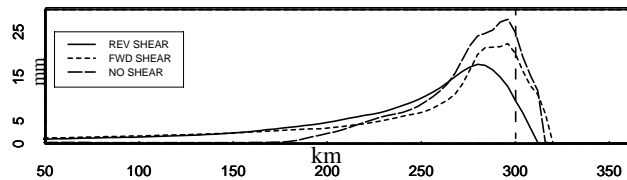
Figure 5. The 6-12 accumulated surface precipitation across a 1500 m barrier (L=25 km) for cases with, no shear (U= 15 m s-1), reverse shear, and forward shear above the barrier crest.

6. PRECIPITATION EFFECIENCY

The windward precipitation efficiency (PE) was calculated for the region upstream (left) of the crest by summing the 6-12 h surface precipitation and dividing by the sink terms of water vapor in the MM5 over this same region. Figure 6 shows the PE averaged for all barrier heights (500-2500 m) for several different N_m, L, and FL runs as a function of wind speed. There is a general decrease in PE with increasing wind speed since more hydrometeors are advected into the lee. However, for the FL500 run, the PE remains relatively unchanged at high windspeeds since the rain generated above the barrier through warm rain processes falls out rapidly (Fig. 2c). The L=25 km and N_m=0.01 s^{-1} runs have lower PEs at higher windspeeds than simulations with larger stability and wider terrain since weaker stability and a narrower barrier favors more precipitation generation above the crest (Fig. 2b), which can advect easily into the lee. The PEs for the surface FL runs (FLSFC) drop more rapidly with increasing wind speed (5 to 30 m s^{-1}) than the higher FL runs since more of the FLSFC precipitation is snow that can spill into the lee. However, the PEs are still larger in the FLSFC than the other experiments for the same wind speed since FLSFC has a lower snow growth region (-15 ^{o}C 700 mb), which favors a larger percentage of precipitation falling out over the windward slope for a relatively wide (L=50 km) barrier (not shown). Even though the PEs are relatively large in the FLSFC, it generates less total surface precipitation than the other experiments since a colder atmosphere holds less moisture (Figs. 2a,d). In contrast, the FL500 run favors more flooding since not only does the atmosphere hold more water vapor, but the lack of lateral hydrometeor advections keep the PEs relatively large at higher wind speeds.
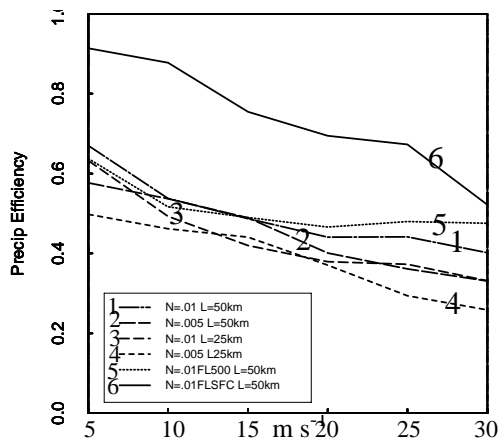
Figure 6. The windward precipitation efficiency averaged for all barrier heights (500-2500 m) as a function of wind speed (m s^{-1}) for the experiments labelled in the inset box.

7. CONCLUSIONS

This study uses the 2-D MM5 to illustrate some of the sensitivities of orographic precipitation to changes in ambient flow (U), moist static stability (N_m), freezing level (FL), terrain height (h_m), and mountain half width (L). The results suggest that the precipitation distribution around a barrier can be strongly dependent on how the terrain-induced gravity wave modifies the mountain circulation. For example, a hydrostatic mountain wave with a small vertical wavelength that tilts upstream with height (favored during weak U, large N_m, and moderately wide terrain) can result in weak sinking motion a few kilometers above the windward slope. This keeps the precipitation shallow and along the windward slope. Both a narrower barrier and weaker stability favor less tilt to the mountain wave or an evanescent wave, resulting in a more collapsed mountain circulation above the crest, and more precipitation spillover (decreased precipitation efficiency). Reverse shear above the crest also favors low-level wave amplification and a windward shift in the precipitation, while forward shear favors a weaker mountain circulation over the crest more advection into the lee. Finally, a freezing level well above crest level collapses the precipitation distribution around the upper-level windward slope, with less lee side spillover, and there is less decrease in the precipitation efficiency with increasing wind speed.

This idealized work is currently being extended to three dimensions using more complex terrain, with the results are being applied to recent field programs such as IPEX and IMPROVE.

8. ACKNOWLEDGEMENTS

9. REFERENCES

Bruintjes, R. T., T. L. Clark, and W. D. Hall, 1994: Interactions between topographic airflow and cloud/precipitation development during the passage of a winter storm in Arizona. *J. Atmos. Sci.*, **51**, 48-67.

Durran, D. R., and J. B. Klemp, 1983: A compressible model for the simulation of moist mountain waves. *Mon. Wea. Rev.*, **111**, 2341-2351.

Jiang, Q, and R.B. Smith, 2002: Microphysical timescales and orographic precipitation. Accepted to *J. Atmos. Sci.*

Klemp, J. B., and D. R. Durran, 1982: An upper boundary condition permitting internal gravity wave radiation in numerical mesoscale models. *Mon. Wea. Rev.*, **111**, 430-444

Neiman, P.J., and co-authors 2002: The statistical relationship between upslope flow and rainfall in the California's coastal mountains: observations during CALJET, accepted to *Mon. Wea. Rev*.

Pandley, G.R., and co-authors, 1999: Precipitation structure in the Sierra Nevada of California during winter. *J. Geophys. Res.*, **104**, 12019-12030.

Sinclair, M.R.,1994: A diagnostic model for estimating orographic precipitation. *J. Appl. Meteor*, **33**, 1163-1175.